

Terahertz ionic Kerr effect: Two-phonon contribution to the nonlinear optical response in insulators

M. Basini,^{1,*} M. Udina^{2,*†}, M. Pancaldi^{3,4}, V. Unikandanunni,¹ S. Bonetti^{1,3} and L. Benfatto²

¹*Department of Physics, Stockholm University, 10691 Stockholm, Sweden*

²*Department of Physics and ISC-CNR, "Sapienza" University of Rome, P.le A. Moro 5, 00185 Rome, Italy*

³*Department of Molecular Sciences and Nanosystems, Ca' Foscari University of Venice, 30172 Venice, Italy*

⁴*Elettra-Sincrotrone Trieste S.C.p.A., 34149 Basovizza, Trieste, Italy*



(Received 5 July 2023; revised 15 November 2023; accepted 2 January 2024; published 18 January 2024)

The THz Kerr effect measures the birefringence induced in an otherwise isotropic material by a strong THz pulse driving the Raman-active excitations of the systems. Here we provide experimental evidence of a sizable Kerr response in insulating SrTiO₃ due to infrared-active lattice vibrations. Such a signal, named the ionic Kerr effect, is associated with the simultaneous excitation of multiple phonons. Thanks to a theoretical modeling of the time, polarization, and temperature dependence of the birefringence, we can disentangle the ionic Kerr effect from the off-resonant electronic excitations, providing an alternative tunable mechanism to modulate the refractive index on ultrashort timescales via infrared active phonons.

DOI: [10.1103/PhysRevB.109.024309](https://doi.org/10.1103/PhysRevB.109.024309)

I. INTRODUCTION

The latest advances in the generation of intense terahertz (THz) field pulses made it possible to investigate the low-frequency counterpart of nonlinear optical phenomena in condensed matter, conventionally studied with visible light, as it is the case for the THz Kerr effect [1–3]. The DC Kerr effect detects a birefringence in an otherwise isotropic material proportional to the square of the applied DC electric field, and it is a standard measurement of the third-order $\chi^{(3)}$ nonlinear optical response of the medium [4]. Basically, the four-wave mixing between the AC probe $E_{AC}(\omega)$ and the DC pump E_{DC} field leads to a nonlinear polarization $P^{(3)} \sim \chi^{(3)} E_{DC}^2 E_{AC}$ (space indexes are omitted). The $P^{(3)}$ in turn modulates the refractive index at the same frequency ω of the AC field, with a space anisotropy set by the direction of E_{DC} . In its optical counterpart, the spectral components around zero frequency of the squared AC field play the same role of the DC component. More recently, THz and optical pulses have been combined in a pump-probe setup to measure the so-called THz Kerr effect [2]. The main advantage over its all-optical counterpart is that intense THz pump pulses can strongly enhance the signal by matching Raman-like low-lying excitations in the same frequency range, such as lattice vibrations [5–8], or collective-modes in broken-symmetry states, as for magnetic [9–13] or superconducting transitions [14–16]. Such a resonant response usually adds up to the background response of electrons, and it can be used to identify the microscopic mechanisms underlying the coupling among different degrees of freedom.

As a general rule, the THz Kerr response, scaling as the THz electric field squared, is not affected by infrared-active

(IR-active) phonons, that correspond to lattice displacements that are linear in the applied electric field. While this is strictly true to first order [17], higher-order processes are not excluded by symmetry. In this work, we demonstrate that the nonlinear excitation of the IR-active soft phonon mode in the archetypal perovskite SrTiO₃ (STO) leads to a sizable contribution to the Kerr signal, which we name the ionic Kerr effect (IKE). STO is a quantum paraelectric [18] showing a large dielectric constant at room temperature ($\epsilon_0 \approx 300$), and with a low-lying phonon mode that progressively softens as the temperature is lowered [19–21]. Such an excitation is an IR-active transverse optical (TO₁) phonon, and it is the same phonon mode which is responsible for the paraelectric to ferroelectric transition upon, e.g., Ca doping [22]. Furthermore, it has been recently pointed out its possible role in the superconducting transition in electron-doped samples [23–25], and the possibility of realizing dynamical multiferrocity upon driving it with circularly polarized THz electric fields [26,27]. Here we show that, besides the well-studied electronic Kerr effect (EKE), due to off-resonant electronic transitions in wide-band insulating STO [28] [Fig. 1(a)], an ionic contribution, associated with the second-order excitation of the TO₁ phonon, is present [Fig. 1(b)]. Such IKE manifests itself with a sizable temperature dependence of the Kerr response, which is unexpected for the EKE in a wide-band insulator. In contrast, the IKE rapidly disappears by decreasing temperature due to the phonon frequency softening far below the central frequency of the pump field. We are able to clearly distinguish between EKE and IKE thanks to a detailed theoretical description of the THz Kerr signal, which we retrieve experimentally as a function of the light polarization and of the pump-probe time delay t_{pp} . So far, the regime of large lattice displacements has been mainly investigated to exploit the ability of infrared-active vibrational modes, driven by strong THz pulses, to anharmonically couple to other phononic excitations [17,29–32]. Our work demonstrates that nonlinear phononic represents also a suitable knob

*These authors contributed equally to this work.

†mattia.udina@uniroma1.it

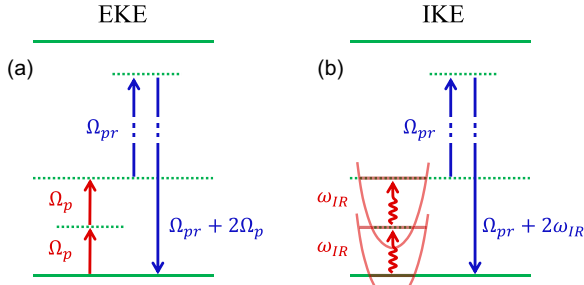


FIG. 1. Terahertz electronic and ionic Kerr effect in a wide-band insulator. In the THz Kerr effect the pump field (red arrows) drives an intermediate state by a sum-frequency two-photons process. Such a state subsequently scatters the visible probe field (blue arrows). In the EKE (a) the intermediate electronic state (dashed line) is virtual, being an insulator, so it relaxes back almost instantaneously giving a $2\Omega_p$ modulation of the emitted light. In the IKE (b) two IR-active phonons (wavy lines) can be used to reach the virtual electronic state [process labeled as (a) in the text], leading to a modulation at $2\omega_{IR}$. This pathway only occurs when the THz pulse is resonantly tuned to the phonon frequency, i.e., when $\omega_{IR} \simeq \Omega_p$.

to manipulate the refractive index of the material, providing potentially an additional pathway to drive materials towards metastable states which may not be accessible at thermal equilibrium [33].

II. EXPERIMENTAL SETUP

Measurements are performed on a 500- μm -thick SrTiO₃ crystal substrate (MTI Corporation), cut with the [001] crystallographic direction out of plane. Broadband single-cycle THz radiation is generated in a DSTMS crystal via optical rectification of a 40-fs-long, 800 μJ near-infrared laser pulse centered at a wavelength of 1300 nm. The near-infrared pulse is obtained by optical parametric amplification from a 40-fs-long, 6.3-mJ pulse at 800-nm wavelength, produced by a 1-kHz regenerative amplifier. As schematically shown in Fig. 2, the broadband THz pulses are filtered with a 3-THz bandpass filter, resulting in a peak frequency of $\Omega_p/2\pi = 3$ THz (with peak amplitude of 330 kV/cm), and focused onto the sample to a spot of approximately 500 μm in diameter. The time-delayed probe beam, whose polarization is controlled by means of a nanoparticle linear film polarizer, is a 40-fs-long pulse at 800-nm wavelength normally incident onto the sample surface. A 100- μm -thick BBO crystal (β -BaB₂O₄, Newlight Photonics) and a shortpass filter are used for converting the probe wavelength to 400 nm and increasing the signal-to-noise ratio in temperature-dependent measurements. The probe size at the sample is approximately 100 μm , substantially smaller than the THz pump. The half-wave plate (HWP) located after the sample is used to detect the polarization rotation of the incoming field induced by the nonlinear response, and a Wollaston prism is used to implement a balanced detection scheme with two photodiodes. The signals from the photodiodes are fed to a lock-in amplifier, whose reference frequency (500 Hz) comes from a chopper mounted in the pump path before the DSTMS crystal. Data are collected as a function of the t_{pp} time-delay as well as a function

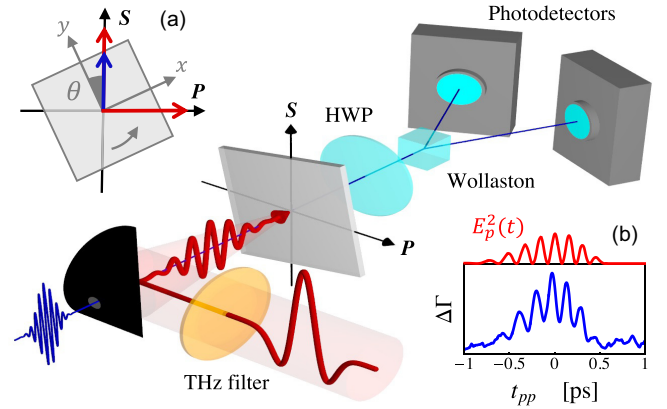


FIG. 2. Schematics of the experimental setup. The THz pulse is in red while the optical probe is in blue. Inset (a): Schematic of the polarization geometry. The sample is rotated in the (S, P) plane, such that the y crystallographic direction forms a variable angle θ with respect to S . Here the probe (blue arrow) polarization is fixed along S , while the pump pulse (red arrow) is polarized along either S or P for linearly polarized light and in both directions for circularly polarized light. Inset (b): Typical time-trace of $\Delta\Gamma$ at fixed $\theta = 67.5^\circ$ (blue line) compared with the intensity profile of the linear pump pulse (red line).

of the angle θ that the probe polarization direction forms with respect to the main crystallographic axes. For convenience, here we assume that the probe beam is kept fixed along the S direction, such that $\mathbf{E}_{pr}(t) = [E_{pr,S}(t) \sin \theta, E_{pr,P}(t) \cos \theta]$, while the pump field \mathbf{E}_p can be either linearly polarized (along S or P direction) or circularly polarized [26], by placing a quarter-wave plate after the bandpass filter (see Appendix A), such that, in general,

$$\mathbf{E}_p(t) = \begin{pmatrix} E_{p,S}(t) \sin \theta + E_{p,P}(t) \cos \theta \\ E_{p,S}(t) \cos \theta - E_{p,P}(t) \sin \theta \end{pmatrix}. \quad (1)$$

In the presence of Kerr rotation, the probe field transmitted through the sample $\tilde{\mathbf{E}}(t)$ acquires a finite P component. The half-wave plate rotates $\tilde{\mathbf{E}}(t)$ by 45° with respect to the P direction and the outgoing signal reaching the two photodetectors (Γ_1, Γ_2) reads [34]

$$\begin{pmatrix} \Gamma_1 \\ \Gamma_2 \end{pmatrix} \propto \begin{pmatrix} 1 & 1 \\ 1 & -1 \end{pmatrix} \begin{pmatrix} \tilde{E}_S \\ \tilde{E}_P \end{pmatrix}. \quad (2)$$

In a pump-probe detection scheme, the use of a chopper on the pump path allows one for measuring, with a lock-in amplifier, the differential intensity $|\Gamma_1|^2 - |\Gamma_2|^2$ with (*on*) and without (*off*) the pump, to obtain

$$\Delta\Gamma = \Delta\Gamma_{\text{on}} - \Delta\Gamma_{\text{off}} \propto (\tilde{E}_S \tilde{E}_P)_{\text{on}} - (\tilde{E}_S \tilde{E}_P)_{\text{off}}. \quad (3)$$

A typical time-trace of $\Delta\Gamma$ for a linearly polarized pump pulse along P and at fixed angle θ is shown in Fig. 2(b), together with $E_p^2(t)$. As we shall see below, the close qualitative correspondence among the two signals is a direct consequence of pumping a band insulator below the band gap. To measure the angular dependence of the response, we then choose t_{pp} at the maximum $\Delta\Gamma$ amplitude, and we record its change as a function of θ . The results are shown in Fig. 3(a) for

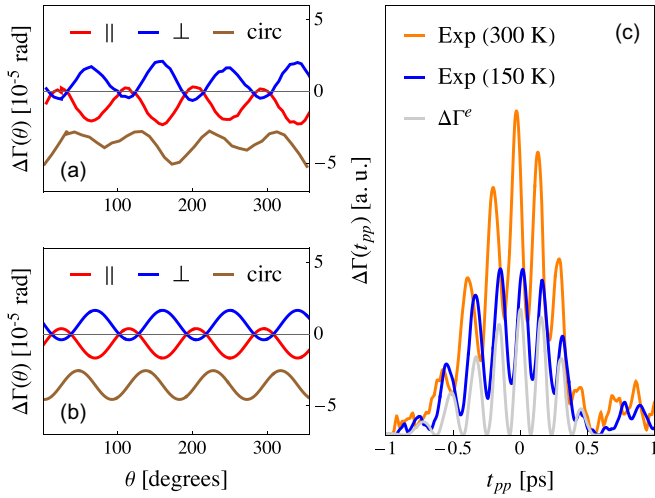


FIG. 3. Polarization and time dependence of the THz Kerr effect. (a) Experimental data as a function of θ at 300 K and $t_{pp} \simeq 0$, where the signal is maximized, in the parallel (\parallel , red curve), cross-polarized (\perp , blue curve), and circular (circ, brown curve) configuration. (b) Corresponding simulations from Eq. (6), accounting for a finite polarization misalignment $\Delta\theta = 5^\circ$ between the pump and probe pulses. (c) Experimental data as a function of t_{pp} at fixed angle $\theta = 67.5^\circ$ in the \perp configuration at 300 K (orange curve) and 150 K (blue curve), compared with the simulated off-resonant electronic contribution $\Delta\Gamma^e$ (gray curve).

both linearly polarized, in either the parallel and the cross-polarized configuration, or circularly polarized pump pulses. In all cases, the signal displays a marked four-fold angular dependency, along with a smaller two-fold periodicity.

III. ELECTRONIC KERR EFFECT

To assess such angular dependence, we first outline the theoretical description of the conventional EKE. The transmitted probe field $\tilde{\mathbf{E}}(t)$ will contain both linear and nonlinear components with respect to the total applied field $\mathbf{E}_p + \mathbf{E}_{pr}$. Since the detection is restricted around the frequency range of the visible probe field, the linear response to the pump can be discarded, as well as higher harmonics of the probe generated inside the sample. We can then retain for $\tilde{E}_S \sim P_S^{(1)}$, with $P_S^{(1)}$ the linear response to the probe along S , while \tilde{E}_P scales as the third-order polarization for a centrosymmetric system, i.e., $\tilde{E}_P \sim P_P^{(3)}$. By decomposing $P_P^{(3)}$ in its (x, y) components one gets

$$\Delta\Gamma \propto \tilde{E}_S P_P^{(3)} = \tilde{E}_S [\cos\theta P_x^{(3)} - \sin\theta P_y^{(3)}]. \quad (4)$$

As mentioned above only contributions linear in E_{pr} to $P_P^{(3)} \simeq \chi^{(3)} E_{pr} E_p^2$ must be retained, where $\chi^{(3)}$ is the third-order susceptibility tensor. By making explicit the space and time dependence one can finally write

$$P_i^{(3)}(t, t_{pp}) = \int dt' \sum_{jkl} E_{pr,j}(t) \times \chi_{ijkl}^{(3)}(t + t_{pp} - t') \tilde{E}_{p,k}(t') \tilde{E}_{p,l}(t'), \quad (5)$$

where we introduce the time shift t_{pp} between the pump and probe pulses, such that $\tilde{E}_p(t + t_{pp}) \equiv E_p(t)$, with $\tilde{E}_p(t)$ and $E_{pr}(t)$ centered around $t = 0$ (see Refs. [35,36] for a similar approach). Since the pump frequency is much smaller than the threshold for electronic absorption ($E_g \sim 3$ eV), the nonlinear electronic response should be ascribed to off-resonant interband excitations, leading to a nearly instantaneous contribution to the third-order susceptibility tensor $\chi^{(3)}$, which can be well approximated by a Dirac delta function, i.e., $\chi_{ijkl}^{(3)}(t) \sim \chi_{ijkl}^{(3)} \delta(t)$, with $\chi_{ijkl}^{(3)}$ a constant value. Under this assumption, Kleinman symmetry for the cubic $m3m$ class appropriate for STO above $T_s \simeq 105$ K assures that the off-diagonal components of the third-order susceptibility tensor have the same magnitude [4]. In the specific case of insulating SrTiO₃, at room temperature one finds $\chi_{iiij}^{(3)} = \chi_{ijji}^{(3)} = \chi_{ijij}^{(3)} \simeq 0.47 \chi_{iiii}^{(3)}$ [37]. Finally, since the measurement at the photodetectors corresponds to the time-averaged field intensity $|\Gamma_i|^2$, one can replace $E_{pr,j}(t)$ in Eq. (5) with its value at $t = 0$, so that the probe pulse acts as an overall prefactor, relevant only for its polarization dependence. With straightforward algebra, and using the decomposition (1) and (4), one obtains the general expression for the EKE

$$\Delta\Gamma^e(t_{pp}, \theta) \propto \frac{1}{4} [\bar{E}_{p,P}^2(t_{pp}) - \bar{E}_{p,S}^2(t_{pp})] \Delta\chi \sin(4\theta) + 2\bar{E}_{p,P}(t_{pp})\bar{E}_{p,S}(t_{pp}) [\chi_{xxyy}^{(3)} + \frac{1}{2} \Delta\chi \sin^2(2\theta)], \quad (6)$$

where $\Delta\chi \equiv \chi_{xxxx}^{(3)} - 3\chi_{xxyy}^{(3)}$. Equation (6) accounts very well for the angular dependence of the signal reported in Fig. 3(a). In particular, for linearly polarized pump pulses, one recovers in Fig. 3(b) the four-fold symmetric modulation, and the overall sign change observed when going from the parallel ($\bar{E}_{p,P} = 0$) to the cross-polarized configuration ($\bar{E}_{p,S} = 0$). Within the same formalism, a finite polarization misalignment $\Delta\theta$ between the pump and probe pulses with respect to S has been considered to explain the small overall (positive or negative) shift of the signal around which the oscillations occur (see Appendix B). When instead circularly polarized pump pulses are applied, the mixed term $\bar{E}_{p,P}\bar{E}_{p,S}$ in Eq. (6) is different from zero and carries a finite isotropic contribution leading to a sizable vertical shift of the signal (even if $\Delta\theta = 0$), which is also reported in Fig. 3(a). Notice that the difference signal between right-handed and left-handed circularly polarized light, as the one measured in Ref. [26], picks up only the $E_{p,P}E_{p,S}$ term of Eq. (6) since a helicity change corresponds to a sign change for one of the two pump components. Beside the expected four-fold symmetric contribution encoded in Eq. (6), we detect a subleading two-fold symmetric contribution, which may be related to an accidental reduced symmetry of the sample or to other effects not captured by our modeling of the whole detection process. Finally, we point out that Eq. (6) provides a generalization for the specular nonlinear anisotropic polarization effect (SNAPE), already reported in cubic crystals for linearly polarized optical pump pulses in the parallel configuration [38,39].

Despite the excellent agreement between the theoretical expression (6) and the measured angular dependence of the signal, marked deviations are observed for the temperature dependence of the signal. Figure 3(c) shows the time-dependent

traces in the cross-polarized configuration at fixed angle θ and two different temperatures. In particular, due to the large value of the band gap, it is hard to ascribe the significant temperature variations observed experimentally to an analogous temperature dependence of the electronic $\chi^{(3)}$ tensor. Indeed, the insulating gap E_g shows a modest temperature renormalization (~ 0.1 eV) in this temperature range [40]. Since, far from the absorption edge the electronic $\chi^{(3)}$ is expected to scale as $\chi^{(3)} \sim 1/E_g^4$ [28], the gap variation could account at most for a 10% increase of the Kerr response between 150 and 300 K. In addition, besides the oscillating component at $\sim 2\Omega_p$, which is consistent with Eq. (6) following the squared pump field in time, a nonoscillating underlying background is found.

IV. IONIC KERR EFFECT

Here we argue that, besides the EKE, the nonlinear response behind the THz Kerr effect admits an additional ionic contribution, where the virtual electronic state is reached via (or decays to) an intermediate two-phonon excitation triggered by two photons of the THz pump pulse, see Fig. 1(b). The frequency of the TO_1 IR-active phonon mode softens from 3.2 to 1.8 THz when lowering the temperature from 380 to 150 K in the cubic phase of STO [21,41]. As a consequence, the IKE is maximized around room temperature, where the frequency spectrum of our THz pump pulse overlaps with the phonon mode, while it gets progressively suppressed by the phonon softening below the pump frequency under cooling. As detailed in Appendix C, two intermediate phonon processes are possible. In one case, denoted by $\Delta\Gamma^{ph,(a)}$, the primary excitation consists in two photons driving two phonons with a strength controlled by the phonon effective charge squared, and only after a virtual electronic state is reached. This process, sketched in Fig. 1(b), can be effectively accounted for by simply replacing each term $\bar{E}_{p,P/S}$ in Eq. (6) for the driving pump field with

$$\bar{F}_{P/S}^{(a)}(t_{pp}) \propto \int dt' D(t') \bar{E}_{p,P/S}(t_{pp} - t'), \quad (7)$$

where $D(t) \equiv \theta(t)e^{-\gamma_T t} \sin(\omega_T t)$ is the (single) phonon propagator, with γ_T and ω_T being the phonon broadening and frequency at temperature T . In the second process, denoted by $\Delta\Gamma^{ph,(b)}$, the intermediate electronic state itself delivers its energy to two IR phonons with opposite momenta, leading to an effective modulation of the $\chi^{(3)}$ tensor. This process can be described by replacing the $\bar{E}_{p,P/S}\bar{E}_{p,P/S}$ product in Eq. (6) with

$$\bar{F}_{P/S,P/S}^{(b)}(t_{pp}) \propto \int dt' P(t_{pp}-t') \bar{E}_{p,P/S}(t') \bar{E}_{p,P/S}(t'), \quad (8)$$

where $P(t) \equiv \theta(t) \coth(\frac{h\omega_T}{2k_B T}) e^{-2\gamma_T t} \sin(2\omega_T t)$ is the two-phonon propagator [42,43]. We point out that $\Delta\Gamma^{ph,(a)}$ has no direct correspondence in conventional Raman experiments and can only be triggered by THz light pulses. Process $\Delta\Gamma^{ph,(b)}$, instead, can be interpreted as the low-frequency time-resolved counterpart of second-order Raman scattering [44]. The full measured quantity, accounting for both the EKE and IKE, then reads

$$\Delta\Gamma = \Delta\Gamma^e + \Delta\Gamma^{ph,(a)} + \Delta\Gamma^{ph,(b)}. \quad (9)$$

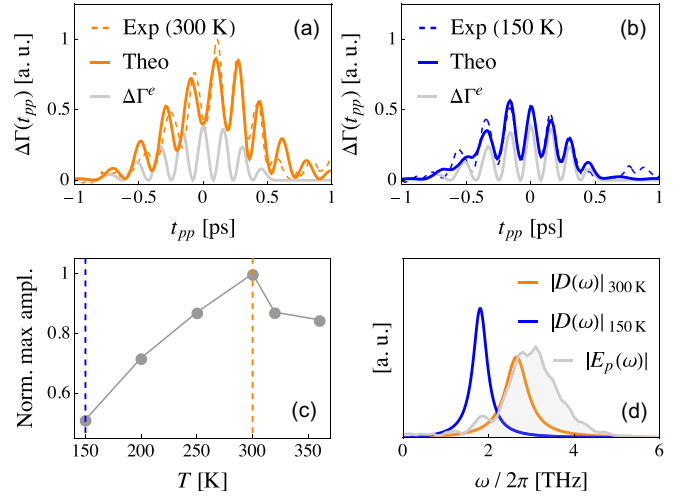


FIG. 4. Comparison between experimental data (dashed lines) and numerical simulations (a), (b) in the absence (gray solid line) and in the presence of phonon-mediated processes at 300 K (orange solid line) and 150 K (blue solid line). (c) Full temperature evolution of the maximum in $\Delta\Gamma$ normalized to its $T = 300$ K value. (d) Spectral content of the linear pump pulse (gray line) compared to the simulated Fourier transform of the IR-active phonon propagator at 300 K (orange line) and 150 K (blue line). Here we set $(\omega_T, \gamma_T)/2\pi \simeq (2.7, 0.3)$ THz at 300 K and $(\omega_T, \gamma_T)/2\pi \simeq (1.8, 0.2)$ THz at 150 K, in agreement with hyper-Raman measurements [21].

For symmetry reasons, we expect the ionic part to preserve the same polarization dependence of the electronic contribution. However, the IKE has a different temporal profile due to the time delay in the intermediate excitation of the IR-active phonons, and a marked T dependence, allowing one to decouple the two effects. Experimental data and theoretical predictions at 150 and 300 K are compared in Figs. 4(a) and 4(b). As expected, even if one assumes a temperature-independent magnitude of the electron-phonon coupling and of the internal pump field, the IKE is strongly reduced when lowering the temperature since the resonant condition between the soft-phonon mode and the pump field is lost, in good agreement with the experimental findings [see Figs. 4(c) and 4(d)]. Above 300 K, instead, the phonon propagator overlaps with the pump spectrum, so that the relative reduction of the signal can be mainly ascribed to the screening of the THz pump pulse (see Appendix D). Nonetheless, both above and below 300 K the presence of a phonon contribution is further supported by a closer inspection of the spectral components of the signal, as detailed in Appendix E. Finally, it is worth noting that, while the velocity mismatch between the pump and probe pulses can influence, in general, the temporal shape of the Kerr signal at optical [36,45] and THz [8] frequencies in thick samples, propagation effects are expected to be negligible in our measurements due to the strong THz absorption close to the TO_1 phonon frequency [17] (see Appendix D).

V. DISCUSSION AND CONCLUSION

In the present paper we demonstrate a direct contribution of the soft IR active TO_1 phonon to the THz Kerr effect

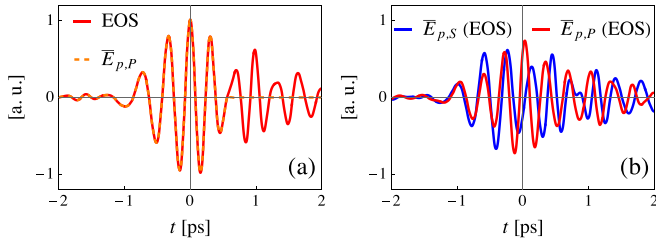


FIG. 5. (a) Electrooptical sampling (EOS) of the linearly polarized terahertz field normalized to its maximum value (red plain line) and the cut time trace used in the simulation (dashed orange line). The maximum field amplitude is 330 kV/cm and the central frequency is $\Omega_p/2\pi = 3$ THz. (b) Electrooptical sampling of the $\bar{E}_{p,S}$ (blue line) and $\bar{E}_{p,P}$ (red line) orthogonal components of the circularly polarized THz pulse, normalized as in (a). Here the maximum field amplitude is 230 kV/cm, with central frequencies $\Omega_{p,P(S)}/2\pi \simeq 3.1(2.9)$ THz.

in insulating STO. The basic mechanism relies on the THz-driven resonant excitation of two IR-active phonons at ω_1, ω_2 frequencies, leading, in general, to a modulation of the refractive index at $\omega_1 \pm \omega_2$. In previously discussed nonlinear phononic effects, the large lattice vibrations provide a way to drive other Raman-active or optically silent lattice degrees of freedom anharmonically coupled to the IR-active resonant mode [17,29–32]. Here we additionally demonstrate that they are responsible for a direct modulation of the conventional EKE. This general paradigm can be further extended to describe materials with different lattice symmetries and electronic properties, opening the avenue for the full exploitation of the IKE to investigate the electron-phonon coupling across various phase transitions. As an example, signatures compatible with the IKE were recently observed in low-temperature KTaO₃ [46]. This system, a parent perovskite material of STO, hosts a low-frequency TO₁ soft phonon mode that is supposed to play a crucial role for its magnetic [47,48] and superconducting [49] response. As such, further characterization of the IKE in this class of materials could provide insightful information on the materials properties in proximity to the ferroelectric and superconducting phase transition.

ACKNOWLEDGMENTS

We are thankful to A. Gherardi and M. N. Gastiasoro for fruitful discussions. M.B. and S.B. acknowledge support from the Knut and Alice Wallenberg Foundation, Grants No. 2017.0158 and No. 2019.0068. M.U. and L.B. acknowledge financial support by EU under MORE-TEM ERC-SYN (Grant Agreement No. 951215) and by Sapienza University under project Ateneo 2022 No. RP1221816662A977.

APPENDIX A: ELECTROOPTIC CHARACTERIZATION OF THZ PUMP PULSES

The characterization of THz pump pulses was performed via electrooptical sampling using a 50- μm -thick GaP crystal cut along the [110] crystallographic direction and placed at the sample position. Multiple THz reflections inside GaP can be observed starting from $t \sim 0.5$ ps in Fig. 5(a). Nonetheless,

this has no influence on the measurements shown in the main text since the large absorption at THz frequencies in STO suppresses multiple reflections below the experimental noise level. Therefore, we considered the cut trace (up to $t \simeq 0.5$ ps) to simulate $\Delta\Gamma$ in the t_{pp} time domain. For comparison, Fig. 5(b) shows the $\bar{E}_{p,S}$ and $\bar{E}_{p,P}$ orthogonal components of the circular pump pulse, obtained by placing a THz quarter-wave plate after the bandpass filter.

APPENDIX B: PUMP-PROBE POLARIZATION MISALIGNMENT

As mentioned in the main text, small deviations from the expected four-fold symmetric periodicity with zero average predicted by Eq. (6) are observed in the experimental data [see Fig. 3(a)]. In particular, when linearly polarized pump pulses are applied, the signal presents an overall positive (in the cross-polarized configuration) or negative (in the parallel configuration) vertical shift. This slight deviation can be explained accounting for a nonzero polarization misalignment $\Delta\theta$ between the pump and the probe pulses with respect to the S direction. More specifically, the pump pulse $E_p(t)$ components (1) can be rewritten as

$$\mathbf{E}_p(t) = \begin{pmatrix} E_{p,S}(t) \sin(\theta + \Delta\theta) + E_{p,P}(t) \cos(\theta + \Delta\theta) \\ E_{p,S}(t) \cos(\theta + \Delta\theta) - E_{p,P}(t) \sin(\theta + \Delta\theta) \end{pmatrix}, \quad (\text{B1})$$

while the probe field still forms an angle θ with respect to the y direction. Following the same steps detailed above, the measured quantity $\Delta\Gamma$, e.g., in the parallel linear configuration ($E_{p,P} = 0$) becomes

$$\Delta\Gamma^e(t_{pp}^*, \theta, \Delta\theta) \propto \bar{E}_{p,S}^2(t_{pp}^*) [-\Delta\chi \sin(4\theta + 2\Delta\theta) + \Delta\chi \sin(2\Delta\theta)], \quad (\text{B2})$$

where the second term accounts for the additional isotropic contribution leading to the observed negative shift of the signal when $\Delta\theta < 0$. Such an explanation implies that the ratio between the overall constant shift and the maximum amplitude of the oscillating component should not depend on the spectral features of the pump pulse. This was experimentally verified by slightly changing the alignment of incoming light in the parallel configuration, without filtering the broad-band THz pulse with the bandpass filter (see Fig. 6). The resulting vertical shift is consistent with the one observed in Fig. 3(a), where instead narrow-band THz pulses were used.

APPENDIX C: EXPLICIT DERIVATION OF PHONON-MEDIATED CONTRIBUTIONS

Here we explicitly show how each contribution to Eq. (9) can be associated with a third-order polarization sharing the same general structure of Eq. (5), i.e., linear with respect to the probe field and quadratic with respect to the pump. From a diagrammatic perspective (see Fig. 7), off-resonant interband electronic transitions leading to the EKE are associated with the bare electronic contribution P^e , coming from process (i), while the intermediate resonant excitation of the IR-active soft-phonon mode, responsible for the IKE, leads to the phonon-mediated contributions $P^{ph.(a)}$ and $P^{ph.(b)}$,

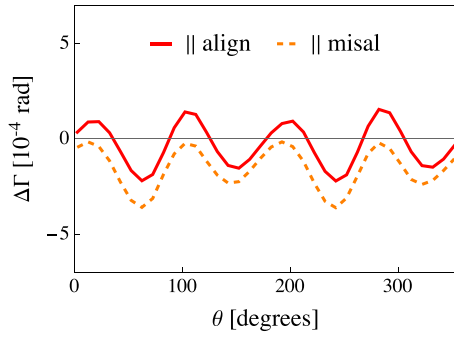


FIG. 6. Experimental data as a function of θ at fixed time-delay t_{pp} , obtained using broadband THz pulses in the parallel (\parallel) configuration. When the pump pulse is aligned along the same direction of the probe (plain red line) the signal oscillates around zero. If one introduces a finite polarization misaligned with respect to the probe direction (here we set $\Delta_\theta \simeq -6^\circ$), instead, an overall vertical shift is observed (dashed orange line), in agreement with Eq. (B2).

associated with process (ii) and (iii), respectively. Each term can be obtained in a straightforward way by means of the effective-action approach, following the same steps detailed, e.g., in Ref. [35] for Raman-active phonon excitations in wide-band insulators.

In particular, the off-resonant electronic contribution P^e can be related with the following action S^e [see Fig. 7(a)], at fourth-order with respect to the external electromagnetic field E :

$$S^e[E] \sim \sum_{ijkl} \int E_{pr,i}(t) E_{pr,j}(t) \chi_{ijkl}^{(3)}(t-t') \times E_{p,k}(t') E_{p,l}(t') dt dt', \quad (C1)$$

which leads to the general Eq. (5) once the partial derivative with respect to the probe field is performed, i.e., $P_i^e \equiv \partial S^e[E]/\partial E_{pr,i}$. When off-resonant (electronic) transitions are considered $\chi_{ijkl}^{(3)}(t) \sim \chi_{ijkl}^{(3)} \delta(t)$. It is then useful to express the effective-action in the frequency domain, where the third-order susceptibility tensor is well approximated with the constant value $\chi_{ijkl}^{(3)}$. By performing the Fourier transform of

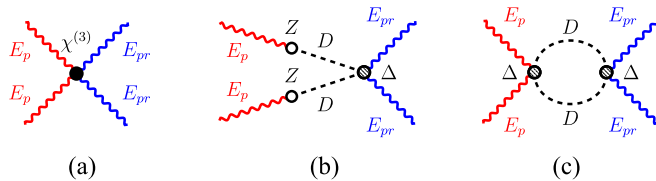


FIG. 7. Diagrammatic representation of the fourth-order contributions to the effective-action $S[E]$, associated with (a) off-resonant electronic transitions and (b) and (c) phonon-mediated resonant excitations. Red (blue) wavy lines represents the pump (probe) field, black dashed lines the phonon propagator. The filled dot represents the nonlinear electron susceptibility $\chi^{(3)}$, empty dots the phonon effective charge Z , and dashed dots the two-phonon effective coupling Δ .

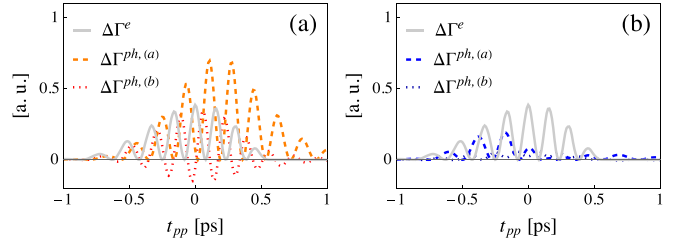


FIG. 8. Simulated single contributions to $\Delta\Gamma(t_{pp})$ at (a) 300 K and (b) 150 K. While the off-resonant electronic contribution $\Delta\Gamma^e$ (plain gray line) is expected to be temperature independent, the phonon mediated processes $\Delta\Gamma^{ph,(a)}$ (dashed lines) and $\Delta\Gamma^{ph,(b)}$ (dotted lines) are strongly suppressed at 150 K, when the resonant condition between the phonon propagator and the pump spectrum is lost [see Fig. 4(d)].

each term, one then finds

$$S^e[E] \sim \sum_{ijkl} \chi_{ijkl}^{(3)} \int E_{p,l}(\Omega_1) E_{p,k}(\Omega_2) \times E_{p,j}(\Omega_3) E_{pr,i}(-\Omega_1 - \Omega_2 - \Omega_3) d\Omega_1 d\Omega_2 d\Omega_3, \quad (C2)$$

where $\Omega_{1,2}(\Omega_3)$ are generic incoming THz (eV) frequencies taken from the pump (probe) pulse.

Focusing now on phonon-mediated processes, in the first case [Fig. 7(b)] two photons from the pump pulse linearly couple to the IR-active phonon mode before reaching the virtual electronic state, leading to the following contribution to the effective-action:

$$S^{ph,(a)}[E] \sim \sum_{ijkl} \int E_{p,l}(\Omega_1) Z_l D(\Omega_1) E_{p,k}(\Omega_2) Z_k D(\Omega_2) \times \Delta_{lkij} E_{pr,j}(\Omega_3) E_{pr,i}(-\Omega_1 - \Omega_2 - \Omega_3) \times d\Omega_1 d\Omega_2 d\Omega_3. \quad (C3)$$

Here $D(\Omega) \equiv \omega_T / [(\Omega + i\gamma_T)^2 - \omega_T^2]$ is the phonon propagator in the frequency domain, Z is related to the phonon effective charge, and Δ gives the effective coupling between the two phonons and the (squared) probe field. While *ab initio* estimates of Z are routinely available in the literature, the estimate of the coupling function Δ requires state-of-the-art extensions of known density functional theory (DFT) codes that have been investigated only recently [44]. As a consequence, a detailed evaluation of the temperature and frequency dependence of Z and Δ goes beyond the scope of this work. Nonetheless, we notice that process (ii) should have, in general, the same polarization dependence of the bare electronic contribution (i) since $\delta\chi_{ijkl}^{(a)} \equiv Z_l Z_k \Delta_{lkij}$ shares, in principle, the same tensor structure of $\chi_{ijkl}^{(3)}$. By then introducing the effective force $F_i^{ph,(a)}(\Omega) \equiv E_{p,i}(\Omega) D(\Omega)$, Eq. (C3) can be rewritten as

$$S^{ph,(a)}[E] \sim \sum_{ijkl} \delta\chi_{ijkl}^{(a)} \int F_l^{(a)}(\Omega_1) F_k^{(a)}(\Omega - \Omega_1) \times E_{pr,j}(\Omega_3) E_{pr,i}(-\Omega - \Omega_3) d\Omega_1 d\Omega d\Omega_3, \quad (C4)$$

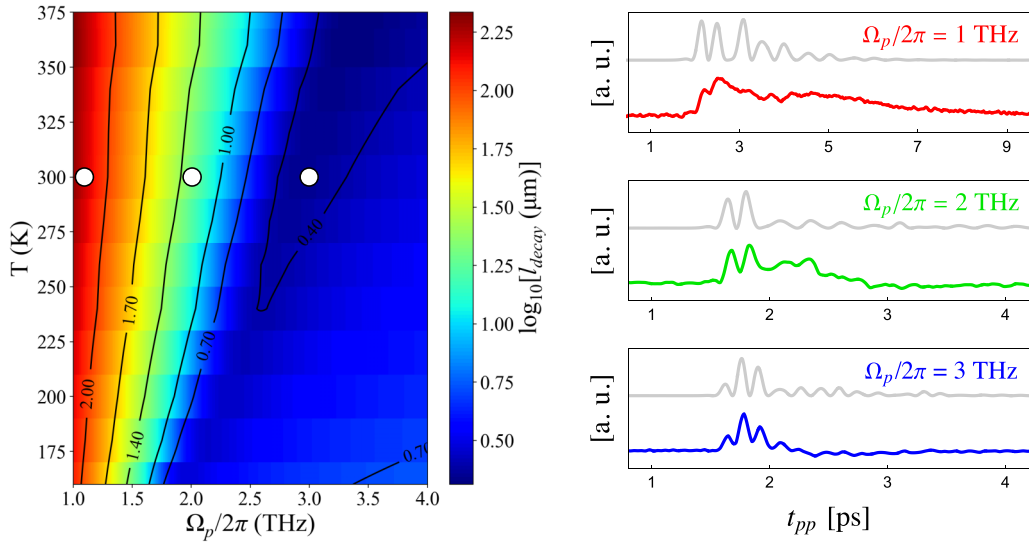


FIG. 9. Left panel: Penetration depth l_{decay} as a function of temperature and frequency as given by Eq. (D3). The temperature-dependent phonon broadening and frequency are taken from Ref. [26]. Right panel: Measured differential intensity $\Delta\Gamma(t_{pp})$ at 300 K compared with the corresponding squared pump pulse $E_p^2(t_{pp})$, with different central frequencies Ω_p (gray lines). To obtain 1-THz pulses, we employed the organic crystal OH1 to generate broadband THz pulses within the frequency range of 0.5 THz to 3 THz, and subsequently, we filtered them using a commercial (TYDEX) 1-THz bandpass filter. To produce pulses centered at 2 and 3 THz, we employed the organic crystal DSTMS to generate broadband THz pulses within the frequency range of 0.5 THz to 6 THz and later filtered them using commercial (TYDEX) 2-THz and 3-THz bandpass filters. The corresponding penetration depths are marked by empty circles in the left panel. All curves are normalized to their maximum value.

with $\Omega = \Omega_1 + \Omega_2$, and the resulting third-order polarization in the time domain reads

$$P_i^{ph,(a)}(t, t_{pp}) \sim \sum_{jkl} \delta\chi_{ijkl}^{(a)} E_{pr,j}(t) \bar{F}_k^{(a)}(t + t_{pp}) \bar{F}_l^{(a)}(t + t_{pp}), \quad (\text{C5})$$

where $\bar{F}_i^{(a)}(t) = \int dt' \bar{E}_{p,i}(t - t') D(t')$, with $\bar{E}_{p,i}(t)$ being centered at $t = 0$.

In the second case, instead, the squared pump field first excites the (virtual) electronic state, which subsequently decays in two IR-active phonons [Fig. 7(c)]. Therefore, the effective coupling Δ describes both the interaction with the pump and with the probe pulses, and the resulting fourth-order contribution to the effective-action scales as $\delta\chi_{ijkl}^{(b)} \equiv$

$\Delta_{ijkl} \Delta_{ijkl}$. In the frequency domain, one then finds

$$S^{ph,(b)}[E] \sim \sum_{ijkl} \delta\chi_{ijkl}^{(b)} \int E_{p,l}(\Omega_1) E_{p,k}(\Omega_2) P(\Omega_1 + \Omega_2) \times E_{pr,j}(\Omega_3) E_{pr,i}(-\Omega_1 - \Omega_2 - \Omega_3) d\Omega_1 d\Omega_2 d\Omega_3, \quad (\text{C6})$$

with $P(\Omega)$ the effective two-phonon propagator [43], i.e.,

$$P(\Omega) \sim \coth\left(\frac{\hbar\omega_T}{2k_B T}\right) \frac{\omega_T}{(\Omega + i0^+)^2 - 4\omega_T^2}, \quad (\text{C7})$$

where we neglect the phonon dispersion for simplicity. One then replaces $i0^+ \rightarrow i2\gamma_T$ to account for the finite phonon lifetime. Both the effective broadening $2\gamma_T$ and the coth term, accounting for the thermal distribution of the phonon population can be explicitly obtained by deriving $P(\Omega)$ at finite temperature T using Matsubara formalism [42]. Going back to Eq. (C6), the corresponding third-order polarization in the time-domain reads

$$P_i^{ph,(b)}(t, t_{pp}) \sim \sum_{jkl} \delta\chi_{ijkl}^{(b)} E_{pr,j}(t) \times \int dt' P(t + t_{pp} - t') \bar{E}_{p,k}(t') \bar{E}_{p,l}(t'). \quad (\text{C8})$$

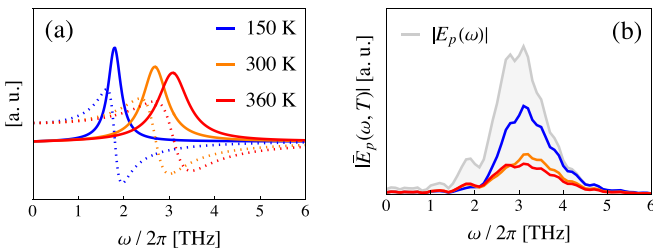


FIG. 10. (a) Real (dotted line) and imaginary (plain line) part of the dielectric function at THz frequencies, as given by Eq. (D2), at 150 K (blue), 300 K (orange), and 360 K (red line). (b) Comparison between the absolute value of the external pump field (gray line) and the spectrum of the estimated internal pump field $|E_p(\omega, T)|$ at 150 K (blue), 300 K (orange), and 360 K (red line).

Starting from Eqs. (C5) and (C8), one then follows the same steps leading to Eq. (6) in the main text to derive $\Delta\Gamma^{ph,(a)}$ and $\Delta\Gamma^{ph,(b)}$, respectively. Notice that, while $\Delta\Gamma^e$ strictly follows the squared pump field in time, $\Delta\Gamma^{ph,(a)}$ follows the squared convolution between the pump and the phonon propagator [see Eq. (C5)], while $\Delta\Gamma^{ph,(b)}$ follows

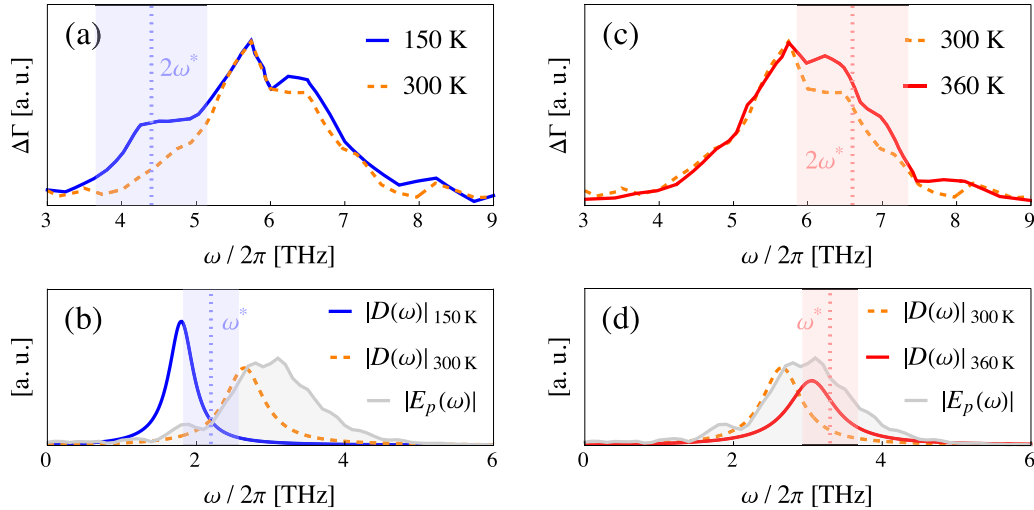


FIG. 11. Temperature evolution of the ionic contribution to the THz Kerr response in the frequency domain. (a) Normalized spectral content of the THz Kerr response at 300 K (orange dashed line) and 150 K (blue plain line). When lowering the temperature, the signal shows an enhancement around $2\omega^* \pm 2\gamma^*$ (blue shaded region), with $\omega^* < \Omega_p$. (b) Pump spectrum (gray curve) compared with the simulated phonon propagator at 300 K (orange dashed curve) and 150 K (blue curve). At 150 K, the overlap between the phonon and the pump is maximized around $\omega^* \pm \gamma^*$ (blue shaded region) that corresponds to half of the frequency scale identified in panel (a). (c) Normalized spectral content of the THz Kerr response at 300 K (orange dashed line) and 360 K (red plain line). When increasing the temperature, the signal shows an enhancement around $2\omega^* \pm 2\gamma^*$ (red shaded region), with $\omega^* > \Omega_p$. (d) Pump spectrum (gray curve) compared with the simulated phonon propagator at 300 K (orange dashed curve) and 360 K (red curve). At 360 K, the overlap between the phonon and the pump is maximized around $\omega^* \pm \gamma^*$ (red shaded region), corresponding in this case to the scale highlighted in panel (c).

the convolution between the two-phonon propagator and the squared pump field [see Eq. (C8)]. Due to the intermediate excitation of the phonon modes, each term shows a different phase factor in the time domain (see Fig. 8), in analogy with sum-frequency ionic Raman scattering [29]. Consequently, their combination leads to interference effects responsible for the temperature-dependent background signal observed in the experiments, in addition to the oscillating component at $\sim 2\Omega_p$.

APPENDIX D: PROPAGATION EFFECTS AND SCREENING OF THE THZ PUMP PULSE

The enhanced value of the refractive index close to the soft-phonon frequency results in a sizable velocity mismatch between the THz pump and the optical probe pulses propagating inside the sample. In particular, at room temperature one finds $n + ik \sim 2.5 + i0$ at the probe frequency [50] and $n + ik \sim 3.8 + i6.4$ at the pump frequency [21,26]. This effect was accounted for in Ref. [1] by integrating the THz-field-induced birefringence associated with the Kerr effect, i.e., $\Delta n(z, t) \propto E_p^2(z, t)$, along the propagating direction z inside the sample

$$\Delta\Phi(t) \propto \int_0^L dz \Delta n(z, t + z/v_{pr}), \quad (\text{D1})$$

where L is the thickness of the sample and v_{pr} the group velocity of the probe pulse. If the THz pump absorption inside the sample can be neglected, i.e., if $k \sim 0$ and the pump field can be rewritten as $E_p(z, t) \rightarrow 2E_p(0, t - z/v_p)/(1 + n)$, one finds that $\Delta\Phi(t)$ does not strictly follow the squared pump pulse $E_p^2(0, t)$ over time. Nonetheless, the soft-phonon mode

leads to a strong THz absorption ($k \gg 0$) in STO, which results in a very small penetration depth l_{decay} of the THz pump field. In particular, at the pump frequency $\Omega_p/2\pi = 3$ THz one finds $l_{\text{decay}} \sim 2.5 \mu\text{m}$ at 300 K and $l_{\text{decay}} \sim 3.6 \mu\text{m}$ at 150 K [26]. Since $l_{\text{decay}} \ll L = 500 \mu\text{m}$, one can replace $E_p^2(z, t) = \delta(z)E_p^2(z, t)$ in Eq. (D1), i.e., the intensity of the incoming pump pulse is sizable only close to the sample surface ($z \simeq 0$), the space integration gets simplified and $\Delta\Phi(t) \propto E_p^2(0, t)$. In other words, the velocity mismatch between the pump and probe pulses is not expected to lead to significant timing modulations over the little length in which the THz field is sizable. This observation had been already pointed out in Ref. [17], where analogous THz Kerr measurements were performed on a 0.5-mm-thick STO sample. To further confirm our expectations, measurements were repeated by changing the central frequency of the THz pump pulse at fixed temperature $T = 300$ K. When lowering the frequency, indeed, one expects the penetration depth to increase, and consequently, the effect of propagation to become more relevant. In particular, by modeling the dielectric function at THz frequencies as done, e.g., in Ref. [20], i.e.,

$$\epsilon(\omega, T) \propto \epsilon_\infty + F^2 \frac{\omega_T^2}{\omega_T^2 - \omega^2 - 2i\gamma_T\omega}, \quad (\text{D2})$$

with ω_T and γ_T the temperature-dependent phonon frequency and phonon broadening, one finds that

$$l_{\text{decay}} = \frac{1}{2\pi\omega k(\omega, T)}, \quad (\text{D3})$$

where $k = \sqrt{(|\epsilon| - \epsilon')/2}$, is $\sim 10(100)$ times greater at 2(1) THz with respect to its 3-THz value (see Fig. 9). The

enhanced values of l_{decay} result in pronounced time variations of the measured signal with respect to the corresponding incoming squared pump pulses $E_p^2(t)$ at $\Omega_p/2\pi = 2$ THz and $\Omega_p/2\pi = 1$ THz. In particular, one finds a long-lasting exponential decay in the time trace which partly (or even fully) buries the Kerr response. These results are fully consistent with the experimental findings reported in Ref. [8], where similar THz Kerr measurements were performed in different perovskite compounds. At the 3-THz pump frequency used in our measurements such spurious effects are actually minimized and this explains why the birefringence actually follows the E_p^2 time dependence.

Beside propagation effects, one can further explore the consequences of a temperature-dependent screening of the THz pulse inside the sample by replacing $E_p(\omega) \rightarrow \tilde{E}_p(\omega, T) = 2E_p(\omega)/[1 + \sqrt{\epsilon(\omega, T)}]$. From Eq. (D2) one immediately notices that the spectral weight of the internal field $\tilde{E}_p(\omega, T)$ gets reduced when the pump pulse is resonant with the phonon-mode due to the enhanced THz absorption. Therefore, one would expect the amplitude of the Kerr response at 300 K to be smaller than at 150 K, in contrast with the experimental findings [see Fig. 4(c)]. This observation further

supports the presence of the ionic contribution to the Kerr response at 300 K that is needed to overcome the detrimental effect of the internal screening on the electronic response. In contrast, for $T > 300$ K the phonon spectrum overlaps with the pump spectrum, leading to a saturation of the phonon contribution and to an overall small decrease of the signal due to the linear screening (see Fig. 10).

APPENDIX E: SPECTRAL CONTENT OF THE IKE

A clear indication of a phonon-mediated contribution to the THz Kerr effect can be obtained by closer comparison between the spectral components of the Kerr response at different temperatures. Indeed, since the phonon peak softens when lowering the temperature, the IKE changes its spectral content. Below 300 K, the IKE survives only at frequencies where the phonon propagator overlaps with the pump spectrum. This leads to an enhancement of the signal at low frequencies as compared to room temperature measurements [Figs. 11(a) and 11(b)]. On the contrary, at 360 K the phonon hardens above the pump frequency and the IKE contribution shifts at higher frequencies [Figs. 11(c) and 11(d)].

-
- [1] M. Sajadi, M. Wolf, and T. Kampfrath, Terahertz-field-induced optical birefringence in common window and substrate materials, *Opt. Express* **23**, 28985 (2015).
- [2] M. C. Hoffmann, N. C. Brandt, H. Y. Hwang, K.-L. Yeh, and K. A. Nelson, Terahertz Kerr effect, *Appl. Phys. Lett.* **95**, 231105 (2009).
- [3] A. A. Melnikov, V. E. Anikeeva, O. I. Semenova, and S. V. Chekalin, Terahertz Kerr effect in a methylammonium lead bromide perovskite crystal, *Phys. Rev. B* **105**, 174304 (2022).
- [4] R. W. Boyd, *Nonlinear Optics*, 3rd ed. (Academic Press, New York, 2008).
- [5] S. Maehrlein, A. Paarmann, M. Wolf, and T. Kampfrath, Terahertz sum-frequency excitation of a Raman-active phonon, *Phys. Rev. Lett.* **119**, 127402 (2017).
- [6] C. L. Johnson, B. E. Knighton, and J. A. Johnson, Distinguishing nonlinear terahertz excitation pathways with two-dimensional spectroscopy, *Phys. Rev. Lett.* **122**, 073901 (2019).
- [7] C. L. Korpa, G. Tóth, and J. Hebling, Mapping the lattice-vibration potential using terahertz pulses, *J. Phys. B: At. Mol. Opt. Phys.* **51**, 035403 (2018).
- [8] M. Frenzel, M. Cherasse, J. M. Urban, F. Wang, B. Xiang, L. Nest, L. Huber, L. Perfetti, M. Wolf, T. Kampfrath, X.-Y. Zhu, and S. F. Maehrlein, Nonlinear terahertz control of the lead halide perovskite lattice, *Sci. Adv.* **9**, eadg3856 (2023).
- [9] T. Kampfrath, A. Sell, G. Klatt, A. Pashkin, S. Mährlein, T. Dekorsy, M. Wolf, M. Fiebig, A. Leitenstorfer, and R. Huber, Coherent terahertz control of antiferromagnetic spin waves, *Nat. Photon.* **5**, 31 (2011).
- [10] S. Baierl, M. Hohenleutner, T. Kampfrath, A. K. Zvezdin, A. V. Kimel, R. Huber, and R. V. Mikhaylovskiy, Nonlinear spin control by terahertz-driven anisotropy fields, *Nat. Photon.* **10**, 715 (2016).
- [11] S. Bonetti, M. C. Hoffmann, M.-J. Sher, Z. Chen, S.-H. Yang, M. G. Samant, S. S. P. Parkin, and H. A. Dürr, THz-driven ultrafast spin-lattice scattering in amorphous metallic ferromagnets, *Phys. Rev. Lett.* **117**, 087205 (2016).
- [12] E. A. Mashkovich, K. A. Grishunin, R. V. Mikhaylovskiy, A. K. Zvezdin, R. V. Pisarev, M. B. Strugatsky, P. C. M. Christianen, Th. Rasing, and A. V. Kimel, Terahertz optomagnetism: Nonlinear THz excitation of GHz spin waves in antiferromagnetic FeBO₃, *Phys. Rev. Lett.* **123**, 157202 (2019).
- [13] E. A. Mashkovich, K. A. Grishunin, R. M. Dubrovin, A. K. Zvezdin, R. V. Pisarev, and A. V. Kimel, Terahertz light-driven coupling of antiferromagnetic spins to lattice, *Science* **374**, 1608 (2021).
- [14] K. Katsumi, N. Tsuji, Y. I. Hamada, R. Matsunaga, J. Schneeloch, R. D. Zhong, G. D. Gu, H. Aoki, Y. Gallais, and R. Shimano, Higgs mode in the *d*-wave superconductor Bi₂Sr₂CaCu₂O_{8+x} driven by an intense terahertz pulse, *Phys. Rev. Lett.* **120**, 117001 (2018).
- [15] K. Katsumi, Z. Z. Li, H. Raffy, Y. Gallais, and R. Shimano, Superconducting fluctuations probed by the Higgs mode in Bi₂Sr₂CaCu₂O_{8+x} thin films, *Phys. Rev. B* **102**, 054510 (2020).
- [16] R. Grasset, K. Katsumi, P. Massat, H.-H. Wen, X.-H. Chen, Y. Gallais, and R. Shimano, Terahertz pulse-driven collective mode in the nematic superconducting state of Ba_{1-x}K_xFe₂As₂, *npj Quantum Mater.* **7**, 4 (2022).
- [17] X. Li, T. Qiu, J. Zhang, E. Baldini, J. Lu, A. M. Rappe, and K. A. Nelson, Terahertz field-induced ferroelectricity in quantum paraelectric SrTiO₃, *Science* **364**, 1079 (2019).
- [18] S. E. Rowley, L. J. Spalek, R. P. Smith, M. P. M. Dean, M. Itoh, J. F. Scott, G. G. Lonzarich, and S. S. Saxena, Ferroelectric quantum criticality, *Nat. Phys.* **10**, 367 (2014).
- [19] M. Kozina, M. Fechner, P. Marsik, T. van Driel, J. M. Glownia, C. Bernhard, M. Radovic, D. Zhu, S. Bonetti, U. Staub, and M. C. Hoffmann, Terahertz-driven phonon upconversion in SrTiO₃, *Nat. Phys.* **15**, 387 (2019).

- [20] P. Marsik, K. Sen, J. Khmaladze, M. Yazdi-Rizi, B. P. P. Mallett, and C. Bernhard, Terahertz ellipsometry study of the soft mode behavior in ultrathin SrTiO₃ films, *Appl. Phys. Lett.* **108**, 052901 (2016).
- [21] H. Vogt, Refined treatment of the model of linearly coupled anharmonic oscillators and its application to the temperature dependence of the zone-center soft-mode frequencies of KTaO₃ and SrTiO₃, *Phys. Rev. B* **51**, 8046 (1995).
- [22] C. W. Rischau, X. Lin, C. P. Grams, D. Finck, S. Harms, J. Engelmayr, T. Lorenz, Y. Gallais, B. Fauqué, J. Hemberger, and K. Behnia, A ferroelectric quantum phase transition inside the superconducting dome of Sr_{1-x}Ca_xTiO_{3-δ}, *Nat. Phys.* **13**, 643 (2017).
- [23] J. M. Edge, Y. Kedem, U. Aschauer, N. A. Spaldin, and A. V. Balatsky, Quantum critical origin of the superconducting dome in SrTiO₃, *Phys. Rev. Lett.* **115**, 247002 (2015).
- [24] M. N. Gastiasoro, J. Ruhman, and R. M. Fernandes, Superconductivity in dilute SrTiO₃: A review, *Ann. Phys. (NY)* **417**, 168107 (2020).
- [25] M. N. Gastiasoro, M. E. Temperini, P. Barone, and J. Lorenzana, Generalized Rashba electron-phonon coupling and superconductivity in strontium titanate, *Phys. Rev. Res.* **5**, 023177 (2023).
- [26] M. Basini, M. Pancaldi, B. Wehinger, M. Udina, T. Tadano, M. C. Hoffmann, A. V. Balatsky, and S. Bonetti, Terahertz electric-field driven dynamical multiferroicity in SrTiO₃, *arXiv:2210.01690*.
- [27] D. M. Juraschek, M. Fechner, A. V. Balatsky, and N. A. Spaldin, Dynamical multiferroicity, *Phys. Rev. Mater.* **1**, 014401 (2017).
- [28] M. Sheik-Bahae, D. J. Hagan, and E. W. Van Stryland, Dispersion and band-gap scaling of the electronic Kerr effect in solids associated with two-photon absorption, *Phys. Rev. Lett.* **65**, 96 (1990).
- [29] D. M. Juraschek and S. F. Maehrlein, Sum-frequency ionic Raman scattering, *Phys. Rev. B* **97**, 174302 (2018).
- [30] A. von Hoegen, R. Mankowsky, M. Fechner, M. Först, and A. Cavalleri, Probing the interatomic potential of solids with strong-field nonlinear phononics, *Nature (London)* **555**, 79 (2018).
- [31] M. Först, C. Manzoni, S. Kaiser, Y. Tomioka, Y. Tokura, R. Merlin, and A. Cavalleri, Nonlinear phononics as an ultrafast route to lattice control, *Nat. Phys.* **7**, 854 (2011).
- [32] A. Subedi, A. Cavalleri, and A. Georges, Theory of nonlinear phononics for coherent light control of solids, *Phys. Rev. B* **89**, 220301(R) (2014).
- [33] A. S. Disa, T. F. Nova, and A. Cavalleri, Engineering crystal structures with light, *Nat. Phys.* **17**, 1087 (2021).
- [34] E. Jiménez, N. Mikuszeit, J. L. F. Cuñado, P. Perna, J. Pedrosa, D. Maccariello, C. Rodrigo, M. A. Niño, A. Bollero, J. Camarero, and R. Miranda, Vectorial Kerr magnetometer for simultaneous and quantitative measurements of the in-plane magnetization components, *Rev. Sci. Instrum.* **85**, 053904 (2014).
- [35] M. Udina, T. Cea, and L. Benfatto, Theory of coherent-oscillations generation in terahertz pump-probe spectroscopy: From phonons to electronic collective modes, *Phys. Rev. B* **100**, 165131 (2019).
- [36] L. Huber, S. F. Maehrlein, F. Wang, Y. Liu, and X.-Y. Zhu, The ultrafast Kerr effect in anisotropic and dispersive media, *J. Chem. Phys.* **154**, 094202 (2021).
- [37] M. J. Weber, *Handbook of Optical Materials*, 1st ed. (CRC Press, Boca Raton, FL, 2002).
- [38] S. V. Popov, Yu. P. Svirko, and N. I. Zheludev, Pump-probe reflective polarization-sensitive nonlinear optics, *J. Opt. Soc. Am. B* **13**, 2729 (1996).
- [39] A. R. Bungay, S. V. Popov, N. I. Zheludev, and Yu. P. Svirko, Specular nonlinear anisotropic polarization effect along four-fold crystal symmetry axes, *Opt. Lett.* **20**, 356 (1995).
- [40] Y.-N. Wu, W. A. Saidi, J. K. Wuenschell, T. Tadano, P. Ohodnicki, B. Chorpeneing, and Y. Duan, Anharmonicity explains temperature renormalization effects of the band gap in SrTiO₃, *J. Phys. Chem. Lett.* **11**, 2518 (2020).
- [41] Y. Yamada and G. Shirane, Neutron scattering and nature of the soft optical phonon in SrTiO₃, *J. Phys. Soc. Jpn.* **26**, 396 (1969).
- [42] G. Caldarelli, M. Simoncelli, N. Marzari, F. Mauri, and L. Benfatto, Many-body Green's function approach to lattice thermal transport, *Phys. Rev. B* **106**, 024312 (2022).
- [43] F. Gabriele, M. Udina, and L. Benfatto, Non-linear terahertz driving of plasma waves in layered cuprates, *Nat. Commun.* **12**, 752 (2021).
- [44] A. Siciliano, L. Monacelli, G. Caldarelli, and F. Mauri, Wigner gaussian dynamics: Simulating the anharmonic and quantum ionic motion, *Phys. Rev. B* **107**, 174307 (2023).
- [45] S. F. Maehrlein, P. P. Joshi, L. Huber, F. Wang, M. Cherasse, Y. Liu, D. M. Juraschek, E. Mosconi, D. Meggiolaro, F. D. Angelis, and X.-Y. Zhu, Decoding ultrafast polarization responses in lead halide perovskites by the two-dimensional optical Kerr effect, *Proc. Natl. Acad. Sci. USA* **118**, e2022268118 (2021).
- [46] X. Li, P. Peng, H. Dammak, G. Geneste, A. Akbarzadeh, S. Prosandeev, L. Bellaiche, and D. Talbayev, Terahertz pulse induced second harmonic generation and Kerr effect in the quantum paraelectric KTaO₃, *Phys. Rev. B* **107**, 064306 (2023).
- [47] R. M. Geilhufe, V. Juričić, S. Bonetti, J.-X. Zhu, and A. V. Balatsky, Dynamically induced magnetism in KTaO₃, *Phys. Rev. Res.* **3**, L022011 (2021).
- [48] R. M. Geilhufe and W. Hergert, Electron magnetic moment of transient chiral phonons in KTaO₃, *Phys. Rev. B* **107**, L020406 (2023).
- [49] C. Liu, X. Zhou, D. Hong, B. Fisher, H. Zheng, J. Pearson, J. S. Jiang, D. Jin, M. R. Norman, and A. Bhattacharya, Tunable superconductivity and its origin at KTaO₃ interfaces, *Nat. Commun.* **14**, 951 (2023).
- [50] A. Dejneka, M. Tyunina, J. Narkilahti, J. Levoska, D. Chvostova, L. Jastrabik, and V. A. Trepakov, Tensile strain induced changes in the optical spectra of SrTiO₃ epitaxial thin films, *Phys. Solid State* **52**, 2082 (2010).